Measurement of mass loss, absorbed energy, and time-resolved reflected power for laser powder bed fusion

David C. Deisenroth[a], Sergey Mekhontsev, Brandon Lane
National Institute of Standards and Technology[b], 100 Bureau Drive, Gaithersburg, MD 20899

ABSTRACT

Laser powder bed fusion processes are driven by scanned, focused laser beams. Along with selectively melting the metal powder, laser energy may be converted and transferred through physical mechanisms such as reflection from the metal surface, heat absorption into the substrate, vaporization, spatter, ejection of heated particles, and heating of the metal vapor/condensate plume that is generated by the laser-metal interaction. Reliable data on energy transfer can provide input for process modeling, as well as help to validate computational models. Additionally, some related process signatures can serve better process monitoring and optimization. Previous studies have shown that the proportion of the transfer mechanisms depend on laser power, spot size, and scan speed. In the current investigation, the energy conservation principle was used to validate our measurement of reflected energy, absorbed energy, and energy transfer by vaporization on bare plates of Nickel Alloy 625 (IN625). Reflected energy was measured using an optical integrating hemisphere, and heat absorbed into the substrate was measured by calorimetry. Transfer from vaporized mass loss was measured with a precision balance and used to establish an upper bound on energy transfer by mass transfer. In addition to measurement of total reflected energy, the reflected laser power was time-resolved at 50 kHz in the integrating hemisphere, which provided insight into the process dynamics of conduction, transition, and keyhole modes.

Keywords: Laser powder bed fusion, laser coupling, energy transfer in laser melting

1. INTRODUCTION

Metal laser powder bed fusion (LPBF) uses selective laser melting of metal powder to additively manufacture a part layer by layer. Complex physical phenomena occur at the laser-metal interaction area due to phase transitions, vapor pressure, surface tension gradients, wetting effects, melt dynamics, and more[1–3]. The energy density applied to the material has a strong effect on the physics that occur in the meltpool, and ultimately on the outcome of the laser melting process.

There are varying definitions of energy density reported in terms of energy divided by length, energy divided by volume, etc., but for the purposes of the current discussion, a strict definition of energy density is not necessary[4,5]. Regardless of definition, it is qualitatively known that the energy density is proportional to applied power and inversely proportional to scan velocity and beam spot size. Therefore, for a given spot size and scan velocity, decreased laser power decreases meltpool width and depth[6].

The energy density applied to the material is also related to the rate of metal vapor generation from the process. At process conditions producing little to no vapor jet, "conduction mode" occurs. Conduction mode is associated with meltpool aspect ratio (depth divided by ½ the width) of less than unity[7]. Among other defects, insufficient energy density is associated with lack of fusion and balling defects in LPBF[8]. At higher energy densities that result in a high rate of vapor generation, the process transitions into "keyhole mode," in which the meltpool depth increases substantially and the aspect ratio can become much greater than unity. A steep increase in laser power/energy absorption is associated with the transition from conduction mode to keyhole mode due to multiple reflections in the deep cavity formed in the meltpool by the vapor recoil pressure[9–11]. Among other defects, excessive or unstable keyholing is associated with residual porosity and loss of volatile alloy components[12,13].

The ability to measure the power and energy transfer that occur in this complex physical process enhances understanding of the process, aids in validation of computational models, and will ultimately help to improve the quality of parts built

---

[a] david.deisenroth@nist.gov; phone 1 301 975-2594

with LPBF. This preliminary investigation sought to measure the energy transfer of the laser melting process via absorption, reflection, and vaporization. Heat energy absorbed by the substrate was measured via calorimetry and evaporated energy was estimated by mass transfer. Reflected laser energy was measured as time-resolved reflected power at 50 kHz, which provided an additional wealth of information about the dynamics of the process in conduction, transition, and keyhole mode.

Measurement of light reflected from laser melting of metal is a very challenging application of reflectometry. The laser-metal interaction area is a highly dynamic reflective surface, which may potentially cause loss of reflected light from the reflectometer when reflected light propagates in the direction with a reduced throughput; the throughput is the ratio of the flux reaching the detector to the input flux from the source. The incident and reflected light can also be scattered and absorbed by the hot metal plume. At the current state of development, these two potentially important losses could not be quantified, although possible avenues for minimizing and/or measuring those effects are in progress. Nevertheless, the sum of the absorbed, reflected, and evaporated energy compared with the input laser energy places bounds on the combined effects of reflected light or energy absorption by the plume.

Laser power reflectometry can complement thermographic measurements and provide additional insight into the complex processes involved in building thin walls and overhangs. Full hemispherical capture of reflected light imposes significant limitations on the process laser incident angles and can find only a limited use in multilayer builds, which will be discussed in the following sections. As an additional benefit, reflected laser power also appears to be a highly useful process monitoring signature for defect detection[14].

2. EXPERIMENTAL METHODS

The experiments reported here were performed in the National Institute of Standards and Technology (NIST) Additive Manufacturing Metrology Testbed (AMMT)[15,16]. The AMMT is a custom LPBF research platform that was designed to be highly configurable for measurement of all aspects of the LPBF process. The AMMT includes a removable carriage that contains the build-well and a large metrology-well, both of which may be moved laterally within the large build chamber. The laser is an Yb-doped fiber laser with emission wavelength of 1070 nm. Laser power delivery can be adjusted from 20 W to more than 400 W, with a 4-sigma diameter (D4σ, representing diameter within which about 95 % of the Gaussian laser power profile is contained) spot size that is adjustable from 45 µm to more than 200 µm. The laser spot can be scanned with full control of the laser scan path/strategy at 100 kHz and laser power control at 50 kHz, with scan velocity from 0 mm/s to more than 4000 mm/s.

In the current investigation, all scans were performed with a velocity of 500 mm/s, a D4σ spot size of 65 µm, and laser power ranging from 50 W to 300W. The working material was rolled and annealed bare plates of Nickel Alloy 625 (IN625)[c] to avoid the measurement complications imposed by powder in this validation experiment. The manufacturer-reported composition of the Alloy 625 material used in this investigation are shown in Table 1.

Table 1. Constituents by mass % of IN625 used in this investigation

Element	Ni	Cr	Mo	Fe	Nb	Mn	Al	Ti
Mass %	60.6	21.98	8.4	4.38	3.44	0.35	0.21	0.21
Element	Si	Cu	C	Co	Ta	P	S	
Mass %	0.19	0.08	0	0.04	0.01	0.01	0.0001	

The surfaces of the plates were ground with 400 grit silicon carbide paper. The samples were assured to be within ±20 µm flatness and levelness of the build plane, resulting in an additional spot size uncertainty of ±1.3 µm due to the known caustic (solid angle of convergence). The following three experimental subsections will describe the approaches used for the three primary measurands: mass loss, laser energy absorption, and reflected laser power. It should be noted that the

[c] Certain commercial entities, equipment, or materials may be identified in this document to describe an experimental procedure or concept adequately. Such identification is not intended to imply recommendation or endorsement by the National Institute of Standards and Technology, nor is it intended to imply that the entities, materials, or equipment are necessarily the best available for the purpose.

reflected power and absorbed energy experiments were done simultaneously, and the mass loss experiments were performed separately on a larger workpiece.

2.1 Mass loss

For measurement of mass loss caused by liquid metal spatter and/or vaporization, IN625 samples with ground surfaces were carefully cleaned with acetone and ethanol to remove debris. The samples were then stored in dry air for 24 hours to remove adsorbed water. The samples were transported in air-tight containers and then weighed on a precision balance. The laser melting process was performed with directional shield gas flow horizontal across the process at about 8 m/s, which was assumed to transport all of the spattered or evaporated material off of the 25 mm × 25 mm × 3 mm sample. After melting, the samples were carefully cleaned and dried again, then weighed.

The primary measurand was mass transfer, but an estimate of how much energy was transferred from the process due to mass loss can also be obtained. The upper bound of energy transfer due to the mass loss is found by assuming that all of the mass was evaporated. Any material that is evaporated absorbs heat energy through five modes in the transition from room temperature solid to superheated vapor, as shown in Equation (1).

$$E_{evap} \approx \Delta m[c_{p,sol}(T_m - T_r) + h_{fus} + c_{p,liq}(T_b - T_m) + h_{vap} + c_{p,vap}(T_{max} - T_b)] \quad (1)$$

Heat is first absorbed by the solid. The solid absorbs energy proportionally to the specific heat ($c_{p,sol}$) and the temperature rises from room temperature (T_r) to the to the melting temperature (T_m). Heat is then absorbed as the latent heat of fusion (h_{fus}) in the phase change from solid to liquid. The material is next heated as a liquid ($c_{p,liq}$) from the melting temperature to the boiling temperature (T_b). The largest energy transition is in the phase change from liquid to vapor (h_{vap}). Finally, the vapor is heated from the boiling temperature (T_b) to the maximum temperature the material reaches (T_{max}).

All values for the material heat capacity and latent heat were taken as the conservatively high values found in available literature. The solid specific heat is temperature dependent and was taken as the average value of about 0.6 J/g·K in the temperature range between room temperature and the melting temperature[17] of about 1300 °C. The latent heat of fusion is highest at the slowest cooling rates and was taken as the conservatively high value[18] of 290 J/g. Information on the heat capacities of IN625 is sparse above the melting point, but using the properties of the majority constituent (Ni) is a reasonable approximation[19]. The liquid latent heat[19] was taken to be 0.73 J/g·K up to Ni boiling point[20] of 2913 °C. Information on the specific heat of metal vapors is very sparse, so it was conservatively assumed that the vaporous specific heat was equivalent to that of the liquid. Precise temperatures of superheated vapor are also unknown, so it was conservatively assumed that the vapor temperatures reach up to 4500 °C. As stated previously, the phase transition from liquid to vapor is the largest energy conversion in the heating process; indeed, this single energy conversion amounts to about double the energy conversion of the solid-liquid phase change and other heating, combined.

Vaporization rates of liquid mixtures are dependent on the concentration of the constituents and the temperature difference between the vaporization temperature of each constituent and the hottest local material. Therefore, additional information is required to precisely calculate how much energy is converted by vaporization of IN625. Nevertheless, it is known that the latent heat of vaporization of the constituents, comprising about 85 % of IN625[21], is within ±5 % of 6.5 kJ/g. The remaining constituents are refractory and trace elements, and so it is a reasonable assumption that the mass loss can be converted to energy within a reasonable margin of uncertainty with this simplified approach. Uncertainty will be discussed in the next subsection.

2.2 Mass loss uncertainty

The balance used to measure the mass loss has a resolution of 0.01 mg and reproducibility of 0.015 mg for a combined mass uncertainty for a given measurement of 0.018 mg, and a mass change uncertainty of 0.025 mg. Estimating the uncertainty of the energy transfer due to the mass loss is far less straightforward, and given the assumptions, an conservative uncertainty of ±30 % was applied. It will be shown in the results section that the energy transferred to mass loss—with conservative assumptions and generous uncertainty assignment—was small compared to the uncertainty of the absorbed energy and reflected energy, precluding the need for further refinement of this energy transfer calculation. The next section will discuss the experimental methods used to measure energy absorbed into the workpiece.

2.3 Absorbed thermal energy

A small sample of about 3 mm × 3 mm × 8 mm was used for the simple calorimetry approach employed here. After surface preparation and attaching a calibrated thermistor, the sample was mounted on low thermal conductivity polymer pedestals. For low laser powers, longer and/or more scan lines were applied to the workpiece and in all cases a temperature rise of between 2.5 °C and 7.5 °C occurred in the workpiece. All scan tracks that were applied in immediate succession were spaced at least 300 µm apart to assure minimal thermal or metallurgical interaction between adjacent scans. The maximum scan time of 110 ms occurred at 50 W laser power. Three-dimensional finite element transient conduction simulations were performed to determine the time required for the workpiece to reach a temperature uniformity within that of the thermistor measurement uncertainty, which was a maximum of 10 s. The data after 10 s were then curve-fitted with Equation (2).

$$T(t) = T_0 + (T_e - T_0)e^{-t/\tau} \tag{2}$$

In Equation (2), $T(t)$ is the fitted temperature function of the thermistor temperature, T_0 is the initial temperature, T_e is the equivalent uniform initial temperature of the workpiece, t is time, and τ is the fitted curve time constant. All curve fits of the experimental data exhibited $R^2 > 0.9999$. Three-dimensional transient conduction simulations were also performed to assure that there was not an inordinate difference in average workpiece temperature decay between the highly non-uniform experimental surface temperature distribution in the initial 10 s and the ideal uniform workpiece surface temperature. The difference was found to be negligible compared to the measurement uncertainty. The equivalent uniform workpiece temperature (T_e) at 0 s was then used to find the absorbed laser energy (E_{abs}) with Equation (3), in which m is the workpiece mass and c_p is the workpiece specific heat.

$$E_{abs} = mc_p(T_e - T_0) \tag{3}$$

2.4 Absorbed thermal energy uncertainty

The uncertainty caused by the heat generation of the thermistor and the uncertainty of the mass of the sample were found to be negligible components of the uncertainty of the absorbed energy. The error in scan time is also believed to be negligible in the current investigation, leaving the remaining components to be those due to the uncertainty in specific heat and temperature rise of the workpiece. The temperature-dependent specific heat of IN625 was reported with standard uncertainty (1σ) of ±1.5 % by Pawel and Williams[22]. The uncertainty of the thermistor was 0.1 °C, resulting in a temperature difference uncertainty of 0.14 °C. These values were then incorporated into the standard propagation of uncertainty for each experiment. The next section will discuss the most challenging measurement of the current investigation, which was measurement of time-resolved reflected power.

2.5 Time-resolved reflected power

An ideal integrating sphere would capture all the light emanating from a source within the sphere, regardless of the direction, collimation, or transient nature of the light. Although an ideal integrating sphere is not possible in practice, appropriate provisions allow for highly efficient capture and measurement of the intensity of integrated light, regardless of how it is emanated. In the current application, the laser power reflected from the laser-melting process was measured.

The design of the integrating apparatus was constrained by the size of the build chamber, the necessary gas flow provisions for laser-metal interaction, and fabrication limitations. Use of a hemisphere instead of a full sphere allowed for a small laser-entrance port size and sample port size, relative to the total integration area, while fitting within the height of the build chamber of the AMMT. The integrating hemisphere was designed using as many best-practices as possible for isotropic throughput[23,24]. A cross-section view of a computer aided design model of the integrating hemisphere is shown in Figure 1, below. As shown, integration is facilitated by a diffuse, barium sulfate coating and with a specular, polished aluminum base. The focused laser light is directed through an elongated port on the top of the hemisphere, about 8° from vertical. The design allows scans to be done in an area of about 3 mm × 20 mm.

Another design constraint is the inert gas atmosphere required for laser melting to reduce detrimental oxidation[25]. Previous studies have shown that directional and inert shield gas flow is essential to facilitate continuous, consistent beam delivery by removing process biproducts that can distort, scatter, and obstruct beam delivery[26–28]. The base of the hemisphere was designed to be 6.7 mm thick due to an incorporated directional shield gas flow and oxygen sampling provision, shown in

Figure 1. In the current investigation, laser scanning occurred in the direction perpendicular to the image plane of Figure 1, perpendicular to the directional shield gas flow.

Upon reaching the sample, some of the laser light is absorbed, causing melting, and some is reflected. The thickness of the base of the dome acts as a baffle and results in a reflected light capture angle of about 135°, as shown in Figure 1. The photodetectors (PD's) were located as close as possible to the equator of the hemisphere. At this location, the base thickness has a beneficial baffle-effect, and prevents deleterious direct viewing of reflected light by the PD's, which would circumvent integration. The base thickness, though, causes a loss of light in the remaining 45° of the hemisphere, which is not integrated. In practice, reflections from the laser-metal interaction at an angle less than 22° from the horizontal are unlikely, but possible, and the associated measurement uncertainty will be discussed in the uncertainty section. The fabricated base, hemisphere interior, and assembled integrating hemisphere are shown in Figure 2.

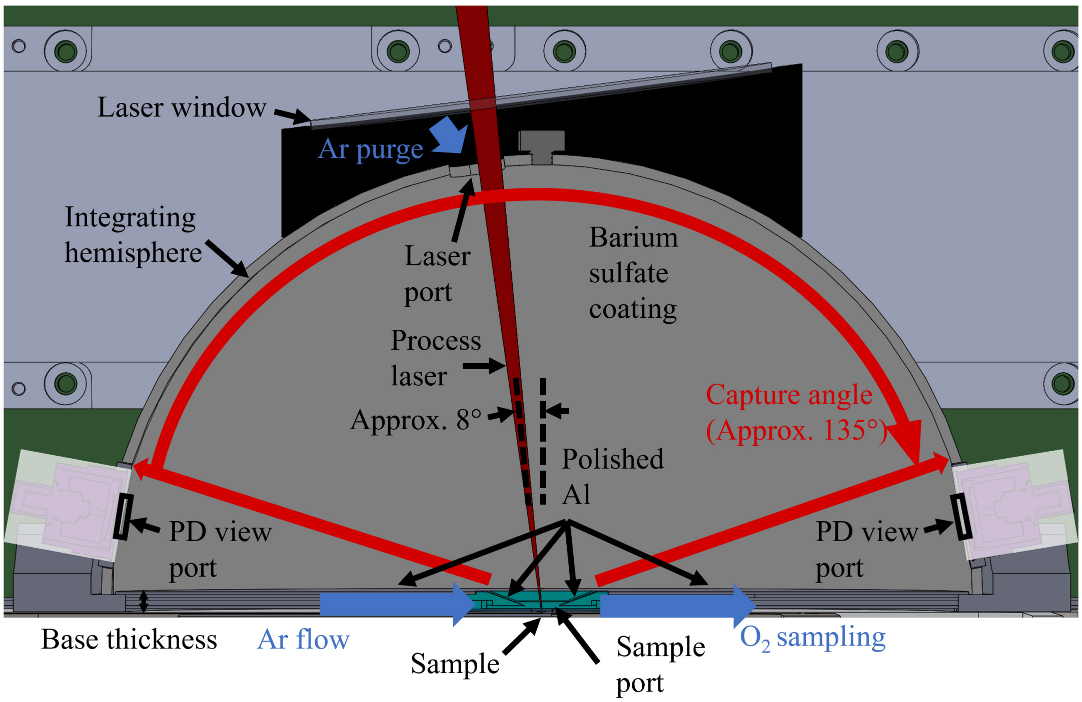

Figure 1. Cross-section view of a computer aided design model of the integrating hemisphere

Figure 2. Images of the fabricated integrating hemisphere (a) specular base, (b) barium sulfate coated hemisphere interior, (c) assembled apparatus in build chamber.

The reflected power captured by the integrating hemisphere reflectometer was measured at a rate of 50 kHz. The PD signal was calibrated with a reflectance standard with reflectance of 0.98 at 1070 nm. The heating laser was defocused and directed onto the specular standard in order to correlate the PD signal with applied power. To convert the transient power measurements into total reflected energy from the process, the power was simply integrated in time, as shown in Equation (4).

$$E_{ref} = \int P_{ref}(t)\, dt \quad (4)$$

2.6 Time-resolved reflected power uncertainty

The light loss due to the laser port and base thickness on the first reflection from the sample were measured by comparing the measured signal with a specular silver standard and a diffuse gold standard. On the first reflection, a specular sample does not result in any port loss or high angle loss. In contrast, a perfectly diffuse sample results in both high angle and port losses. After accounting for the reflectivity of the samples, it was found that the discrepancy was 2.5 % in intensity. Combined with the applied power (calibration) uncertainty of 2.5 %, the resulting reflected power uncertainty is 3.5 %. This value is taken as the estimated (Type B) standard uncertainty for the reflected power[29].

Throughput mapping of the inside of the hemisphere was performed to assure that, aside from the known losses, the relative location-dependent throughput of the integrating surface was uniform. The throughput is the ratio of the flux reaching the detector to the input flux from the source. Throughput mapping was performed with illumination around the equator of the hemisphere via 36 LED's at 850 nm wavelength. The reflectance of barium sulfate is expected to be similar in value at the LED and laser wavelengths. A photodetector was then placed at the entrance port and a gimbal-mounted mirror was mounted at the sample port. The mirror was aimed at a representative number of locations across the inside of the hemisphere. Although the mapping is not a perfect representation of the actual application, it is a good representation because of the similarity of reflectance at the LED and laser wavelengths and the known reciprocity of directional-hemispherical and hemispherical-directional measurements. Therefore, the measurements assure that there are no significant, unforeseen non-uniformities on the integrating surface.

As shown in Figure 3, the throughput uniformity of the surface is within ±1 % across the majority of the surface. It should be kept in mind that due to the Mercator projection; the corresponding true surface area is reduced by the cosine of the vertical angle. Thus, the entrance port area appears significantly greater than its true relative surface area. As was anticipated, significant losses and errors occur at a vertical angle of less than 22°.

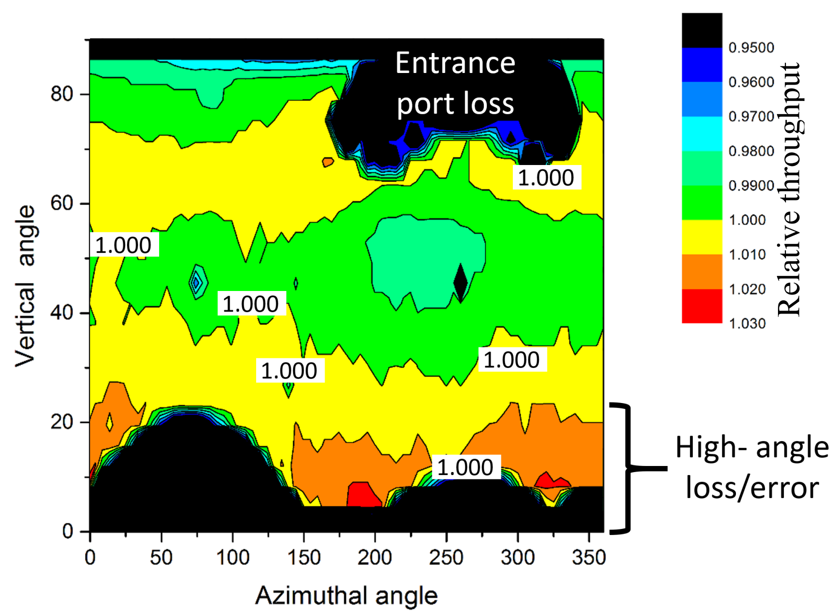

Figure 3. Relative throughput of the hemispherical integrating surface, shown in a Mercator projection.

At the current state of development, there are some significant unknowns about the character of the reflection from the laser-metal interaction. Depending on the applied energy density, the laser incident surface may be steeply inclined, and can reflect light forward along the scan direction, upward, or opposite to the scan direction[30,31]. The laser melting process is also highly dynamic, causing the reflective surface to rapidly change in time.

Further complicating matters, suspended vapor/condensate plume directly above the workpiece surface may also scatter and absorb both the incident and reflected laser light[32]. Incident laser light absorbed by the plume does not reach the workpiece and would not be measured by either calorimetry or reflectometry, which means that the fidelity of neither calorimetry nor reflectometry is compromised by incident laser light absorbed by the plume. Fidelity is retained because the energy reaching the workpiece is reduced and that would be accurately measured. However, plume absorption may affect the laser energy density applied to the surface, and thereby affect the melt pool formation and characteristics.

Incident laser light scattered by the plume may potentially be integrated and registered as light reflected from the workpiece, causing an erroneously high reflected light measurement. Laser light reflected from the workpiece that is then absorbed by the plume may cause an erroneously low measurement of the reflected power. Finally, laser light reflected from the workpiece that is then scattered by the plume would aid in integration, and therefore, not affect reflected power measurement. In summary, incident laser light scattering and reflected light absorption have counteracting erroneous effects on reflectometry, which are not yet well understood.

Therefore, with reflectometry alone, a significant portion of the reflected laser light could be lost or detected as erroneous reflection. Hence, the current investigation has sought to measure the sum of the measured reflected laser energy, the heat absorbed by the substrate, and the energy transfer to vaporization as a preliminary investigation into the magnitude of the combined measurement error and process energy loss to the plume.

The results of mass and energy transfer by vaporization or spatter, time-resolved reflected laser power, calorimetry, and combined energy balance will be presented in the following sections. It should be noted that the results shown in the "time-resolved reflected power" section were obtained with a more rudimentary experimental reflectometer setup than was described in this section, so the absolute values of normalized reflected power have greater uncertainty and port loss than the rest of the results. Nevertheless, the results are used to demonstrate the wealth of data that can be obtained with time-resolved non-contact reflectometry at 50 kHz.

3. RESULTS AND DISCUSSION

Examples of the melt tracks generated from the combined absorption and reflected power experiments are shown first, followed by the results of the mass and energy transfer due to vaporization. Then, time-resolved reflected power measurements with 20 mm long tracks with examples in conduction, transition, and keyhole mode are shown. And finally, the primary result of this effort, the combined energy balance obtained with the three forms of measurement, are discussed.

3.1 Melt tracks from reflectometer and calorimetry experiments

Examples of the melt tracks generated from the combined absorption and reflected power experiments are shown in Figure 4. The laser power at which the tracks were scanned are labeled. The tracks at each power were scanned from left to right and the track succession is from top to bottom. The lines at each laser power were scanned in immediate succession while the temperature of the workpiece was measured. In other words, each set of tracks labeled by applied laser power in Figure 4 represents an energy input that caused a temperature rise in the workpiece that was recorded until the workpiece cooled back to room temperature. It may be observed that the tracks of, for example, 50 W and 100 W are "interleaved," which was simply for convenience. Approximately equivalent energy (about 2 J) was input at each laser power, hence three tracks at 100 W were applied for equivalent energy input to a single 300 W track, and the three 50 W tracks are twice as long as the 100 W tracks. The track length ranged from 3 mm to 7 mm and the spacing between immediately successive tracks was at least 300 µm.

Cross-sections of the tracks formed for this study were not made, but the modes of laser-metal interaction are known from cross-sections performed by previous researchers under comparable conditions, as well as the characteristic changes in absorption[10]. The 60 W laser power resulted in conduction mode. At this power, the melt tracks were narrow and the solidified end of track shapes were short. In transition mode, at 100 W, the melt tracks are significantly wider and the solidified track ends were an elongated teardrop shape. At 300 W in keyhole mode, the melt track is the widest and the solidified track end was a highly elongated teardrop. In all cases, the melt tracks were visibly uniform and repeatable.

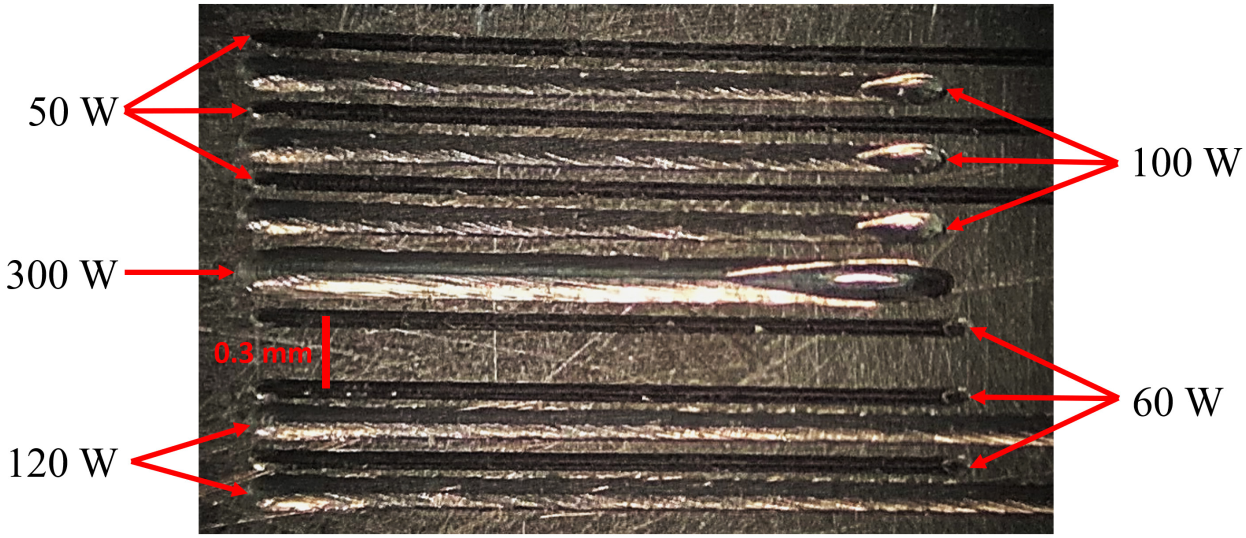

Figure 4. Melt tracks generated in the combined absorption and reflected power experiments with applied laser power pointing to tracks scanned in immediate succession

3.2 Mass and energy transfer due to vaporization

The measured mass transfer divided by distance for three laser powers and the estimated upper bound of normalized energy transfer from that mass are shown in Figure 5. Starting with 50 W, it can be observed that any mass loss was below the measurable limit, and therefore, energy transfer was also below the measurable limit. The mass loss divided by distance increased approximately linearly from no measured amount at 50 W, up to a value of 0.67 mg/m at 300 W.

The mass loss is about three times greater at 300 W compared to 100 W, causing the normalized estimated energy loss in transition mode and keyhole mode to be in close proximity. With the conservative estimate that all of the mass was transferred by vaporization and with an estimated uncertainty of 30 %, the total energy portion converted by mass loss was still less than 0.015 of the input energy. Therefore, because this transfer of energy was on the same order as the measurement uncertainty of both absorbed and reflected energy, energy loss due to mass transfer was taken as an additional 1.5 % uncertainty in the total energy balance for this preliminary investigation.

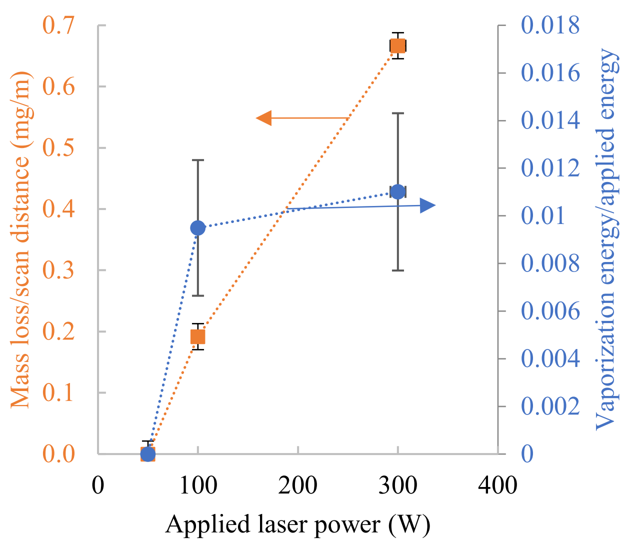

Figure 5. Mass transfer at varying laser power and estimated normalized energy transfer due to mass transfer

3.3 Time-resolved reflected power

The reflected power results were obtained with 20 mm long tracks under the same process parameters (spot size, scan speed, surface finish, etc.) as the rest of the results in this investigation, but with slightly greater uncertainty than the remainder of the results. Nevertheless, the results demonstrate the wealth of data that can be obtained with time-resolved non-contact reflectometry at 50 kHz, as shown in shown in Figure 6. In these results, three tracks were scanned in immediate succession and spaced 0.5 mm apart to avoid thermal and metallurgical interaction.

The reflected power from applied laser powers of 50 W, 100 W, and 200 W are shown in Figure 6 a, b, and c, respectively. Starting with Figure 6 a, about 0.50 of the laser power was reflected during each of the three scans. At the initiation of each 50 W track there is a slight overshoot with higher reflected laser power portion, up to 0.53 after the initial rise time. Overall, the conduction mode tracks exhibited very low variability along the length of the track.

In Figure 6 b, the 100 W tracks are in transition mode and show very high variability in reflected power along the length of the tracks. This high variability of reflected light in transition mode was observed in all experiments in this investigation and appears to be related to establishment of the vapor depression. The tracks exhibit nearly a 60 % difference in the reflected light portion at initiation of the track compared with the constant value of about 0.27 reached after the first 8 mm

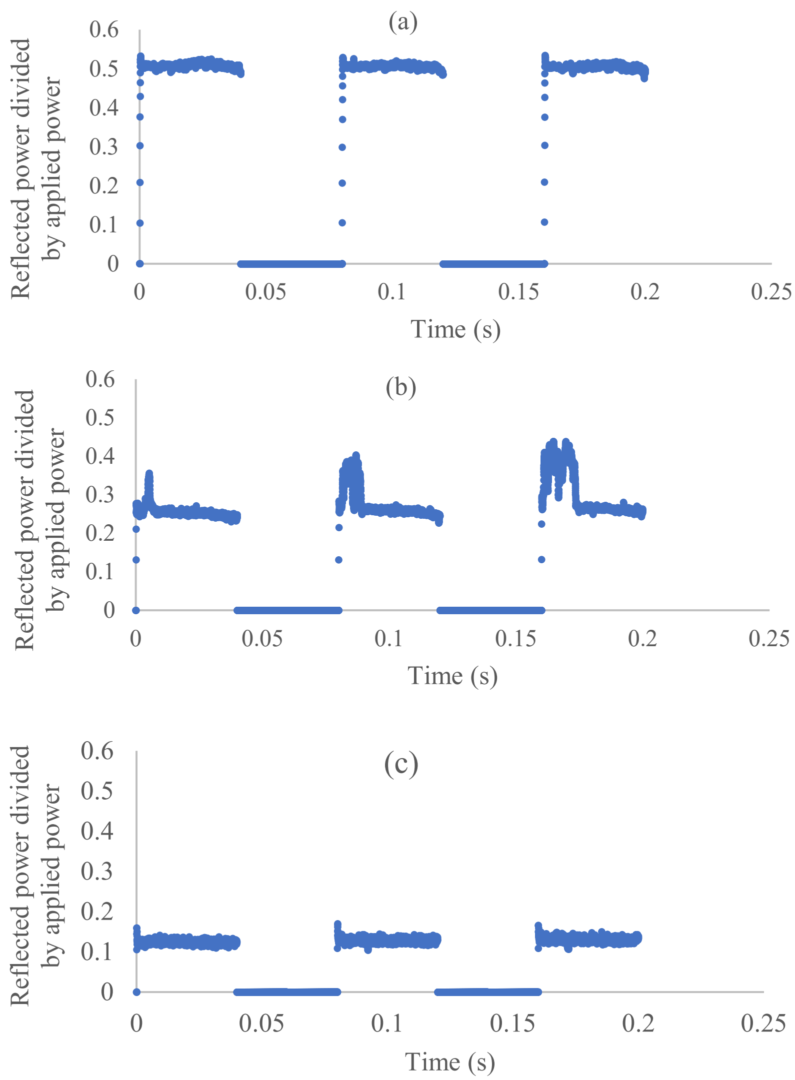

Figure 6. Time-resolved reflected power normalized by applied power. Each scan consists of three 20 mm long tracks scanned at (a) 50 W, (b) 100 W, and (c) 200 W

of the track. It is currently unknown whether the apparent increase in track establishment length with each track is systematic or stochastic and will be investigated in the future.

Finally, in Figure 6 c, the 200 W tracks are in keyhole mode. At initiation of the track, the reflected light portion overshoots to 0.18 after the short initial rise time, then reaches an average value of about 0.125. In keyhole mode, the reflected light portion showed what appears to be a periodic fluctuation between 0.11 and 0.14 along the length of each scan. The frequency of such periodic fluctuations may be reported in the future.

3.4 Energy sum

The normalized reflected laser energy, absorbed heat energy, and their sum are shown as a function of applied laser power in Figure 7, with vaporization energy based on mass loss measurements added as a 1.5 % uncertainty component of the energy sum uncertainty. The energy values normalized by the applied laser energy indicate the relative proportion of reflected and absorbed energy, which would ideally sum to unity if all of the input energy were measured. It should be noted that the dotted lines in Figure 7 are not curve fits, but simply reference lines to guide the eye.

The trend and values of normalized absorbed energy are consistent with previous results under comparable conditions[9,10]. At 50 W laser power the absorbed energy portion is about 0.34, increasing to only 0.40 at 80 W. Then, the absorbed energy portion jumps to about 0.60 at 100 W and increases steadily to about 0.90 at 300 W. This jump in absorption at 100 W is associated with transition mode, while the low absorption is associated with conduction mode and the high absorption is associated with keyhole mode. The largest discrepancy between tests performed with the same laser power occurred in transition mode at 100 W, which appears to be related to the highly dynamic nature of absorption on the bare plates in transition mode, as was shown in Figure 6. Conversely to the portion of absorbed energy, the normalized reflected energy portion starts at 0.60 at 50 W, drops to about 0.30 at 100 W, and then the reflected energy portion falls to 0.07 at 300 W.

Turning now to the non-melting tests performed with an approximately 300 μm defocused laser spot under the same conditions, it can be seen from Figure 7 that a portion of 0.97 of the ideal energy sum was measured with 4.5 % uncertainty. The uncertainty is reported with 1σ confidence, indicating 68 % certainty that the measured value lies within the error

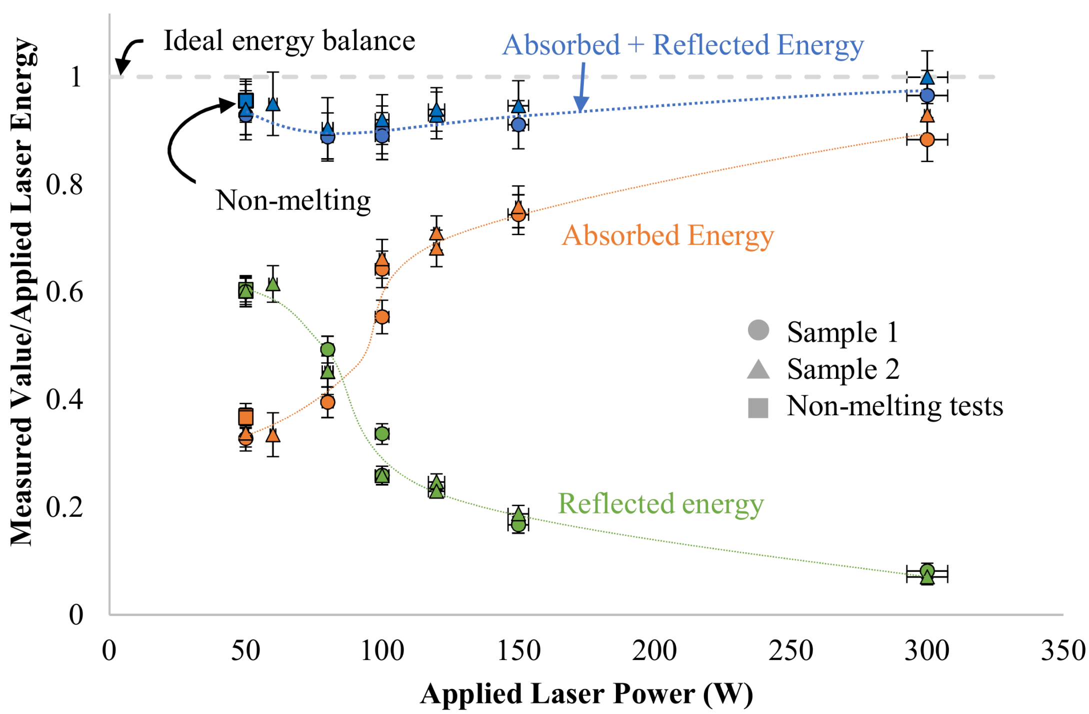

Figure 7. Reflected energy, absorbed energy, and the measured energy sum as a function of applied laser power. The dotted lines are to guide the eye along each data locus. Vertical and horizontal error bars indicate the combined standard uncertainty representing approximately 68 % confidence

bars. Therefore, the ideal energy balance was measured within the uncertainty under non-melting conditions, that likely generate a specular reflection.

In tests that caused melting, the error bars (which include energy transfer due to mass loss as an uncertainty) are within 1.5 % or less of the ideal energy balance, indicating that essentially all of the energy was measured at 50 W and 300 W. The maximum discrepancy between the ideal energy balance occurred at 80 W, at which between 7 % to 16 % of the applied energy was left unmeasured. In the current state of development, it is unclear whether this unmeasured energy is due to losses from the reflectometer (port losses or high-angle losses), or if a larger portion of the energy is converted to heating the ambient gas above the process in transition mode.

4. CONCLUSIONS

We are reporting the first known to us measurements of time-resolved reflected laser power from laser-matter interaction under conditions of interest for LBPF, which was accompanied by measurements of mass loss and absorbed laser energy. These three measurements performed together are meant to offer the modeling community a comprehensive set of data related to the laser-matter interaction processes. The measurement process can be streamlined so that such data sets can be developed for multiple materials and process parameters of interest.

In this investigation, tracks were laser melted into bare plates of IN625 with process conditions of interest for LPBF. The scan speed was 500 mm/s, the D4σ spot size was 65 µm, and the laser power was varied from 50 W to 300 W. Under the conditions tested, it was found that less than 1.5 % of the input energy was converted to vaporization. With time-resolved (50 kHz) reflected laser power measurements, it was observed that laser coupling is highly dynamic in transition mode, and periodic fluctuations in coupling were observed in keyhole mode.

Conservation of energy was confirmed to be measured in non-melting tests with a defocused beam. In tests with melting, conservation of energy was measured to be within 1.5 % or less of the 1σ error bars at the lowest and highest laser power. The maximum discrepancy between the measured and ideal energy balance occurred in transition mode, at which between 7 % to 16 % of the applied energy was left unmeasured. In the current state of development, it is unclear whether this unmeasured energy is due to port losses or high-angle losses in the integrating hemisphere, or if a larger portion of the energy is converted to heating the ambient gas/vapor/condensate above the process in transition mode.

Further developments depend on the interest of the community and can be directed either toward perfection of the reported measurements (such as reducing the uncertainties), expanding the functionality (e.g. measuring in the multilayer build condition with a powder layer), or connecting these measurands with the process outcomes.

ACKNOWLEDGEMENTS

The authors wish to thank to Mark Stoudt of the NIST Materials Measurement Laboratory for use of the precision balance for measuring mass loss. The authors also wish to thank you to Leonard Hanssen of NIST Physical Measurement Laboratory (PML) for aid in reflectometry uncertainty and analysis. The authors further wish to thank Brian Simonds of NIST PML for technical discussions. Finally, the authors with to thank Vladimir Khromchenko of NIST PML and Daniel Cardenas-Garcia of the National Metrology Center of Mexico for their work in characterizing the reflectometer.

REFERENCES

[1] Bidare, P., Bitharas, I., Ward, R. M., Attallah, M. M. and Moore, A. J., "Fluid and particle dynamics in laser powder bed fusion," Acta Materialia 142, 107–120 (2018).

[2] Wang, Y., Xing, L., Li, K., Yu, C., Ma, J., Liu, W. and Shen, Z., "Band-Like Distribution of Grains in Selective Laser Melting Track Under Keyhole Mode," Metallurgical and Materials Trans. B 50(2), 1035–1041 (2019).

[3] Keshavarzkermani, A., Marzbanrad, E., Esmaeilizadeh, R., Mahmoodkhani, Y., Ali, U., Enrique, P. D., Zhou, N. Y., Bonakdar, A. and Toyserkani, E., "An investigation into the effect of process parameters on melt pool geometry, cell spacing, and grain refinement during laser powder bed fusion," Optics & Laser Tech. 116, 83–91 (2019).

[4] Scipioni Bertoli, U., Wolfer, A. J., Matthews, M. J., Delplanque, J.-P. R. and Schoenung, J. M., "On the limitations of Volumetric Energy Density as a design parameter for Selective Laser Melting," Materials & Design 113, 331–340 (2017).
[5] Fabbro, R., "Scaling laws for the laser welding process in keyhole mode," J. Materials Processing Tech. 264, 346–351 (2019).
[6] Ghosh, S., Ma, L., Levine, L. E., Ricker, R. E., Stoudt, M. R., Heigel, J. C. and Guyer, J. E., "Single-track melt-pool measurements and microstructures in Inconel 625," JOM 70(6), 1011–1016 (2018).
[7] Eagar, T. and Tsai, N., "Temperature-Fields Produced by Traveling Distributed Heat-Sources," Weld. J. 62(12), S346–S355 (1983).
[8] Yadroitsau, I., [Selective laser melting: Direct manufacturing of 3D-objects by selective laser melting of metal powders], Lambert Academic Publishing (2009).
[9] Trapp, J., Rubenchik, A. M., Guss, G. and Matthews, M. J., "In situ absorptivity measurements of metallic powders during laser powder-bed fusion additive manufacturing," Applied Materials Today 9, 341–349 (2017).
[10] Ye, J., Khairallah, S. A., Rubenchik, A. M., Crumb, M. F., Guss, G., Belak, J. and Matthews, M. J., "Energy Coupling Mechanisms and Scaling Behavior Associated with Laser Powder Bed Fusion Additive Manufacturing," Adv. Eng. Materials, 1900185 (2019).
[11] Simonds, B. J., Sowards, J., Hadler, J., Pfeif, E., Wilthan, B., Tanner, J., Harris, C., Williams, P. and Lehman, J., "Time-Resolved Absorptance and Melt Pool Dynamics during Intense Laser Irradiation of a Metal," Phys. Rev. Applied 10(4), 044061 (2018).
[12] Elmer, J. W., Vaja, J., Carlton, H. D. and Pong, R., "The effect of Ar and N2 shielding gas on laser weld porosity in steel, stainless steels, and nickel," Weld. J. 94(10), 313s–325s (2015).
[13] Aboulkhair, N. T., Everitt, N. M., Ashcroft, I. and Tuck, C., "Reducing porosity in AlSi10Mg parts processed by selective laser melting," Additive Manufacturing 1, 77–86 (2014).
[14] Coeck, S., Bisht, M., Plas, J. and Verbist, F., "Prediction of lack of fusion porosity in selective laser melting based on melt pool monitoring data," Additive Manufacturing 25, 347–356 (2019).
[15] Lane, B., Mekhontsev, S., Grantham, S., Vlasea, M., Whiting, J., Yeung, H., Fox, J., Zarobila, C., Neira, J. and McGlauflin, M., "Design, developments, and results from the nist additive manufacturing metrology testbed (AMMT)," Proc. Solid Freeform Fabrication Symp., 1145–1160 (2016).
[16] Yeung, H., Neira, J., Lane, B., Fox, J. and Lopez, F., "Laser path planning and power control strategies for powder bed fusion systems," Proc. Solid Freeform Fabrication Symp., 113–127 (2016).
[17] Haynes International., "HAYNES® 625 alloy: Principal Features," H-3073F (2018).
[18] Tinoco, J. and Fredriksson, H., "Solidification of a Modified Inconel 625 Alloy under Different Cooling Rates," High Temperature Materials and Processes 23(1), 13–24 (2011).
[19] Mills, K. C., [Recommended values of thermophysical properties for selected commercial alloys], Woodhead Publishing (2002).
[20] Lide, D. R., [CRC Handbook of Chemistry and Physics, 90th Edition], Taylor & Francis (2009).
[21] Zhang, Y., Evans, J. R. G. and Yang, S., "Corrected Values for Boiling Points and Enthalpies of Vaporization of Elements in Handbooks," J. Chem. Eng. Data 56(2), 328–337 (2011).
[22] Pawel, R. E. and Williams, R. K., "Survey of physical property data for several alloys," ORNL/TM--9616, Oak Ridge National Lab. (1985).
[23] Hanssen, L. M., Cagran, C. P., Prokhorov, A. V., Mekhontsev, S. N. and Khromchenko, V. B., "Use of a high-temperature integrating sphere reflectometer for surface-temperature measurements," Int. J. Thermophysics 28(2), 566–580 (2007).
[24] Snail, K. A. and Hanssen, L. M., "Integrating sphere designs with isotropic throughput," Applied Optics 28(10), 1793–1799 (1989).
[25] Ahn, J., He, E., Chen, L., Dear, J. and Davies, C., "The effect of Ar and He shielding gas on fibre laser weld shape and microstructure in AA 2024-T3," J. Manufacturing Processes 29, 62–73 (2017).
[26] Malekipour, E. and El-Mounayri, H., "Common defects and contributing parameters in powder bed fusion AM process and their classification for online monitoring and control: a review," Int. J. Adv. Manufacturing Tech. 95(1–4), 527–550 (2018).
[27] Ladewig, A., Schlick, G., Fisser, M., Schulze, V. and Glatzel, U., "Influence of the shielding gas flow on the removal of process by-products in the selective laser melting process," Additive Manufacturing 10, 1–9 (2016).

[28] Anwar, A. B. and Pham, Q.-C., "Effect of inert gas flow velocity and unidirectional scanning on the formation and accumulation of spattered powder during selective laser melting," Proc. of the 2nd Intl. Conf. on Progress in Additive Manufacturing, Singapore (2016).
[29] Taylor, B. N. and Kuyatt, C. E., "Guidelines for evaluating and expressing the uncertainty of NIST measurement results," NIST Technical Note 1297, National Institute of Standards and Technology (1994).
[30] Zheng, H., Li, H., Lang, L., Gong, S. and Ge, Y., "Effects of scan speed on vapor plume behavior and spatter generation in laser powder bed fusion additive manufacturing," J. Manufacturing Processes 36, 60–67 (2018).
[31] Ly, S., Rubenchik, A. M., Khairallah, S. A., Guss, G. and Matthews, M. J., "Metal vapor micro-jet controls material redistribution in laser powder bed fusion additive manufacturing," Sci. Reports 7(1), 4085 (2017).
[32] Shcheglov, P. Y., Gumenyuk, A. V., Gornushkin, I. B., Rethmeier, M. and Petrovskiy, V. N., "Vapor–plasma plume investigation during high-power fiber laser welding," Laser Phys. 23(1), 016001 (2012).